Dual-photoelastic-modulator-based polarimetric imaging concept for aerosol remote sensing

David J. Diner,[1,*] Ab Davis,[1] Bruce Hancock,[1] Gary Gutt,[1] Russell A. Chipman,[2] and Brian Cairns[3]

[1]Jet Propulsion Laboratory, California Institute of Technology, Pasadena, California 91109, USA
[2]College of Optical Sciences, University of Arizona, Tucson, Arizona 85721, USA
[3]NASA Goddard Institute for Space Studies, New York, New York 10025, USA

*Corresponding author: David.J.Diner@jpl.nasa.gov

Received 7 August 2007; accepted 8 October 2007;
posted 18 October 2007 (Doc. ID 86206); published 3 December 2007

A dual-photoelastic-modulator- (PEM-) based spectropolarimetric camera concept is presented as an approach for global aerosol monitoring from space. The most challenging performance objective is to measure degree of linear polarization (DOLP) with an uncertainty of less than 0.5% in multiple spectral bands, at moderately high spatial resolution, over a wide field of view, and for the duration of a multiyear mission. To achieve this, the tandem PEMs are operated as an electro-optic circular retardance modulator within a high-performance reflective imaging system. Operating the PEMs at slightly different resonant frequencies generates a beat signal that modulates the polarized component of the incident light at a much lower heterodyne frequency. The Stokes parameter ratio $q = Q/I$ is obtained from measurements acquired from each pixel during a single frame, providing insensitivity to pixel responsivity drift and minimizing polarization artifacts that conventionally arise when this quantity is derived from differences in the signals from separate detectors. Similarly, $u = U/I$ is obtained from a different pixel; q and u are then combined to form the DOLP. A detailed accuracy and tolerance analysis for this polarimeter is presented.

OCIS codes: 120.5410, 230.2090, 280.1100.

1. Introduction

Aerosols, tiny particles suspended in the air, have profound and myriad influences on the Earth's climate, hydrological cycle, air quality, and human health. Climate and environmental policies require reliable models of aerosol impacts, and these models can only be validated and constrained by accurate measurements. Satellite remote sensing, with its global perspective, has a key role in measuring the distribution, radiative impact, and microphysical properties of aerosol-laden air masses. However, parameters such as aerosol optical depth (AOD), single-scattering albedo (SSA), particle size distribution, particle shape, refractive index, and vertical distribution jointly govern backscattered radiances; and as a consequence, remote sensing retrievals are typically underconstrained.

Recent remote sensing advances have used a variety of approaches to deal with this indeterminacy, each sensitive to different aspects of aerosol microphysics [1]. Multispectral techniques, e.g., from the Moderate Resolution Imaging Spectroradiometer (MODIS) on the Terra and Aqua satellites, make use of spectral scattering efficiency to provide sensitivity to particle size along with AOD [2,3]. Inclusion of bands in the visible and shortwave infrared (SWIR), in particular, provides discrimination between fine and coarse size modes. Near-ultraviolet mapping from the Earth Probe Total Ozone Mapping Spectrometer (TOMS) and the Ozone Monitoring Instrument (OMI) on Aura is beneficial because most surfaces are dark at these wavelengths, and the interaction between aerosol and Rayleigh scattering provides enhanced sensitivity to aerosol absorption and height [4,5].

Multiangle intensity imaging, e.g., from the Envisat Advanced Along-Track Scanning Radiometer (AATSR and its precursors), and the Terra Multi-

0003-6935/07/358428-18$15.00/0

Table 1. Salient Aerosol Sensor Characteristics

Instrument	Spatial Resolution (km)	Along-Track Angular Range	Spectral Range (nm)	Polarimetric Uncertainty	Global Coverage Time (days)
MISR	0.275–1.1	70° fore–70° aft	446–866	NA	9
MODIS	0.250–1.0	NA[a]	469–2130	NA	2
AATSR	1–2	0°, 55° fore	550–1610	NA	5
TOMS/OMI	20–40	NA	270–500	NA	1
POLDER	6–7	60° fore–60° aft	443–910	2%	2
APS	6–20	60° fore–60° aft	412–2250	0.2%	NA
MSPI	0.275–1.1	70° fore–70° aft	355–1610	0.5%	4

[a]NA = not applicable.

angle Imaging SpectroRadiometer (MISR), take advantage of differences in the spatial and angular reflectance signatures of the surface and atmosphere to retrieve AOD over a wide variety of surfaces [6–9]. Multiangle radiometry also provides constraints on particle size and sphericity by sampling the particle scattering phase function [10,11]. Oblique slant paths through the atmosphere enhance sensitivity to aerosols and thin cirrus, and stereoscopy makes possible the geometric retrieval of aerosol plume-top heights when sufficient spatial contrast is present to facilitate pattern matching [12].

Multiangle polarimetric data at visible and shortwave infrared wavelengths provide compositional proxy information through retrieval of the real part of the aerosol refractive index, n_r, and particle size mode variances, each with greater sensitivity than intensity measurements alone. These capabilities have been demonstrated experimentally with the airborne Research Scanning Polarimeter (RSP) [13,14], through theoretical sensitivity studies [15], and with the spaceborne Polarization and Directionality of Earth's Reflectances (POLDER) instrument [16]. POLDER spatial resolution is 6–7 km, with degree of linear polarization (DOLP) uncertainty of ~2% [17]. The Aerosol Polarimeter Sensor (APS) instrument for NASA's Glory mission, using similar design concepts as the airborne RSP, will provide very accurate multiangle polarimetric measurements (linear polarization uncertainty ~0.2%), but in a coarse resolution (6–20 km, depending on view angle), nonimaging mode [18]. APS spatial coverage is limited to a single along-track scan over a swath measuring ~6 km in width in the nadir.

Integration of multispectral, multiangular, and polarimetric sensing approaches into a single instrument enables a synergistic reduction in retrieval indeterminacies [19], providing the best chance of meeting the requirements for climate studies (equivalent to radiative forcing uncertainty less than 1 W m^{-2}), and air quality studies, for which moderately high spatial resolution improves aerosol-cloud discrimination and makes possible measurement of urban aerosol gradients. Imaging over a broad swath provides global coverage within a matter of days, encompassing the typical residence time of aerosols and providing sampling on temporal scales valuable for data assimilation. A broad swath also makes possible the capture of unusual events, and enables frequent sampling of validation and field campaign sites. An integrated imager is one component of a future mission concept endorsed by the National Research Council Decadal Survey for Earth Sciences [20]. Our approach, the Multiangle SpectroPolarimetric Imager (MSPI), brings together key attributes of the instruments cited above (see Table 1).

The most difficult requirement for MSPI, given the current state of technology, is the 0.5% DOLP tolerance. This requirement allows for the accurate simultaneous retrieval of AOD and particle size when combined with accurate multiangle–multispectral radiance measurements. The polarization measurements provide particular sensitivity, of ± 0.01, to n_r, thus providing information regarding particle composition. Polarimetry acts synergistically with intensity measurements to reduce the level of indeterminacy in the retrieval of aerosol properties, and also has the potential to reduce uncertainties in AOD retrievals by about a factor of 2 relative to intensity-only multiangle measurements.

2. Instrument Architecture

A. Predecessor Instrument Configuration

The MISR instrument [21] provides the starting point for definition of the MSPI instrument architecture. MISR acquires multiangle radiance imagery from a set of nine pushbroom cameras, with the forward and backward viewing cameras paired in a symmetrical arrangement at a fixed set of view angles. Relative to the Earth's surface, the along-track angles are nominally 0° (nadir) and 26.1°, 45.6°, 60.0°, and 70.5° forward and backward of nadir. During a 7 min interval, each point within the instrument swath is viewed in succession by the nine cameras as the spacecraft flies overhead.

The MISR lenses are superachromatic, seven-element, refractive $f/5.5$ telecentric designs, and the focal lengths vary with view angle in order to preserve cross-track sample spacing. A double-plate Lyot depolarizer is incorporated into each of the cameras to render them polarization insensitive. Focal lengths range from 59 to 124 mm, keeping cross-track pixel size and sample spacing to 250 m for the nadir cam-

era and 275 m for the off-nadir cameras. Along-track footprints depend on view angle, ranging from 214 m in the nadir to 707 m at the most oblique angle. However, sample spacing in the along-track direction is 275 m in all cameras as a consequence of the 40.8 ms line repeat time of the charge-coupled device (CCD) readouts. Each MISR camera contains four CCD line arrays with 21 μm detector pitch, and a focal plane filter assembly is mounted above the CCDs to define the four optical bandpasses, centered at 446, 558, 672, and 866 nm. Coregistration of the data in both band and angle is accomplished in ground data processing [22].

B. Incorporation of Polarimetric Imaging

The MISR optical design requires modification to accommodate the MSPI spectral and polarimetric requirements. A depolarizer cannot be used, and the new design must have low polarization aberrations, particularly low diattenuation, and must have high transmittance from the ultraviolet (UV) to the SWIR. To reduce the time it takes to cover the entire globe from low Earth orbit, the MSPI cameras have twice the cross-track field of view (FOV) of the MISR cameras (approximately ±31° for the shortest focal length lens). In the along-track direction, a ±1° FOV accommodates the suite of detector lines filtered to various spectral bands and polarimetric states.

The polarization state of light incident on an optical system can be represented by the four Stokes parameters (I, Q, U, V), where the component I is the total intensity; Q represents the excess of light at 0° orientation to a specified plane relative to the intensity at 90°; U is the excess of intensity at 45° relative to 135°; and V is the excess of right-handed circular polarization to left-handed circular polarization. In terms of the Stokes parameters, the degree of linear polarization, DOLP, is

$$\mathrm{DOLP} = \sqrt{(Q/I)^2 + (U/I)^2} = \sqrt{q^2 + u^2}, \tag{1}$$

which depends only on the relative ratios q and u, given by

$$q = Q/I, \tag{2}$$

$$u = U/I. \tag{3}$$

For natural targets illuminated by sunlight, circular polarization is anticipated to be less than 0.1% of the total intensity. The MSPI instrument concept measures only the linear polarization components. Nonetheless, the optical system is designed to minimize instrumental circular polarization, as well as cross talk of V into Q and U.

Many factors affect the polarimetric accuracy of an imager [23], including polarization sensitivity of the optics (termed instrumental polarization), requiring accurate calibration; the use (in most design configurations) of different detectors whose signals are subtracted to measure polarization (with implications for detector cross calibration); and spatial displacements on the ground of the locations where different polarization orientations are measured, giving rise to so-called "false polarization" or "polarization artifacts." Spatial misregistration between the measurements comprising a polarization measurement is particularly problematic in the presence of scene gradients.

Snapshot or spectrum channeling imagers use optical elements—gratings, prisms, or birefringent crystals—to encode the polarization state within a spatially or spectrally varying signal recorded on an area array detector [24–28]. These approaches are elegant but typically have high polarization uncertainties, and can introduce errors in the presence of rapid spatial or spectral variability. Other methods include polarimeters that optically divide the incoming light using beam splitters; however, optical aberrations and scattered light can be problematic. Division-of-aperture polarimeters, which employ multiple analyzers operating side-by-side, have fewer optical components, but their main drawback is the use of different detectors to reconstruct the Stokes vector. Small errors in calibration between the detectors could make it difficult to achieve a verifiable and reliable DOLP measurement uncertainty of 0.5%. For example, the MISR pushbroom cameras acquire multispectral, nonpolarimetric observations using adjacent line arrays overlain by filters passing different wavelengths [21]. The analog of this measurement approach for polarimetry would be to overlay different line arrays with analyzers in different orientations. MISR experience shows that the data from different lines within a single camera can be digitally coregistered to better than 1/10 of a pixel; however, even after extensive analysis of the in-flight data, residual uncertainties in the radiometric cross calibration between channels are of the order of 1%–2% [29]. Such an arrangement would by itself risk violating the 0.5% DOLP requirement, and some additional means of reducing errors is needed.

In scanning instruments detector cross calibration can be achieved using a simple unpolarized calibration source that the detectors see through the same optical path as when viewing the Earth. This approach is used for APS and a similar method has been implemented in the RSP, which has demonstrated a relative gain calibration of better than 0.05%. For a nonscanning pushbroom imager such as MSPI, we take advantage of the fact that only relative measurements q and u are required. The detector cross-calibration problem is circumvented by introducing a time-variable retardance into the optical path to modulate the polarized component of the incoming light. The unmodulated portion of the signal encodes intensity; the modulated component encodes Q or U, depending on the orientation of the polarization analyzer overlaying the detector array. Both Q and I are obtained from the same detector (similarly for U and I), so the ratios $q = Q/I$ and $u = U/I$ are independent of system transmittance and detector gain variations from pixel to pixel, or over time. If the modulation is too slow, then for a changing scene (as is the case for

a moving space platform) the detector does not view the same target as the different measurements are acquired. This can be mitigated by rapidly modulating the signals with periods shorter than the line repeat time (~40 ms from low Earth orbit, corresponding to an along-track resolution of 275 m). Using the MISR architecture as a starting point for the MSPI concept, spectral and polarimetric separation is accomplished using filters and analyzers above the individual line arrays. Modulation of the polarization state at a frequency of 25 Hz results in a complete cycle of the modulated waveform within each 40 ms line repeat interval. Detector readout occurs at a rate sufficient to sample the modulated signal, e.g., by acquiring 32 samples of 1.25 ms duration each.

In principle, the required temporal retardance modulation can be accomplished with a rotating wave plate; however, vibrations at the required rotation speeds (a few thousand revolutions per minute) and bearing wear over multiyear operation could introduce beam wobble and optical wavefront phase shifts. Ferroelectric liquid crystal devices can provide a nonmechanical solution with tuning speeds of 30–250 μs [30], however, the chromophores typically transmit only over a limited spectral bandpass, e.g., 400–700 nm, and the MSPI instrument must work over a much broader range. Consequently, our preferred approach is to use photoelastic modulators (PEMs).

PEMs have been in use for over 25 years as a method of polarization modulation in a variety of research and industrial applications [31]. Their operation is based on the principle that uniform optical materials such as glass become birefringent when compressed along one axis. This is commonly referred to as stress-induced birefringence, or the photoelastic effect. A variable retarder can be constructed by compressing optical glass but a large amount of power is needed to slowly modulate the stress-induced birefringence. Practical PEMs make use of mechanically resonant oscillation at a high mechanical quality factor Q (not to be confused with the second Stokes parameter Q) of 10^3–10^4, reducing the power requirement to less than 0.5 W. By coupling a piezoelectric transducer (PZT) to a glass or fused-silica bar, a standing sound wave that oscillates at the bar's fundamental frequency is induced, causing a rapid modulation of the birefringence. The benefits of PEMs include low operating voltages, large apertures, and wide angular acceptance [32]. Because PEMs are constructed from glass or fused silica, transmittance over a wide spectral range is straightforward. Polarimetric sensitivities (i.e., precision) of about three parts in 10^6 have been obtained for solar astronomy applications [33–35].

Typical PEM frequencies are in the tens of kilohertz for glass elements several centimeters in size. This is much higher than the 25 Hz modulation rate MSPI requires. Our solution places two PEMs oscillating at slightly different frequencies in series within the optical path. The result is a high-frequency "carrier" waveform, modulated at the much slower heterodyne, or beat frequency governed by the small difference in resonant frequencies of the two PEMs. A line readout integration time of ~1.25 ms is sufficiently long that the high-frequency carrier signal is averaged out, but sufficiently fast that dozens of samples of the modulated waveform are acquired every image frame. Section 3 presents the theory behind this approach.

3. Polarimetry Using Photoelastic Modulators: Theory

A. Single Photoelastic Modulators

A PEM is constructed to vibrate in one of two modes. For rectangular bars operating in the one-dimensional mode, the modulation frequency ω, is [36]

$$\omega = \frac{\pi}{L}\sqrt{\frac{E}{\rho(1-\sigma^2)}}, \tag{4}$$

where E is the Young's modulus, ρ is the density, σ is the Poisson's ratio, and L is the length of the bar. For fused-silica bars with L between 3 and 15 cm the frequency ranges from 100 to 20 kHz. The stress-induced retardance δ is given by

$$\delta(x,\ t) = \delta'\ \sin(\pi x/L)\sin(\omega t - \varphi), \tag{5}$$

where δ′ is the amplitude of the retardance oscillation, t is time, φ is the phase relative to an arbitrary time origin, and the spatial variable x extends from 0 to L.

Square PEMs, which are constructed to vibrate in the two-dimensional mode, have a modulation frequency given by

$$\omega = \frac{\pi}{L}\sqrt{\frac{E}{\rho(1+\sigma)}}, \tag{6}$$

and a stress-induced retardance given by

$$\delta(x,\ y,\ t) = \delta'\ \sin(\pi x/L)\sin(\pi y/L)\sin(\omega t - \varphi), \tag{7}$$

where the spatial variables x and y extend from 0 to L. The advantage of the two-dimensional mode is that the amplitude of the retardance oscillation is doubled for the same driving power. In practice, the corners of the square PEM are cut to form an octagon. The PEM is mounted at these trimmed corners, taking advantage of the fact that these locations are vibrational-displacement nodes. Because the amplitude of the modulation peaks at the center of the element and falls to zero at the edges, only the central portion is used to attain maximum efficiency (e.g., the central 1.6 cm of a 6.4 cm square element). If the PEM is placed in the pupil plane of an optical system, then the effective amplitude reduces to

$$\delta(t) = \delta_0\ \sin(\omega t - \varphi), \tag{8}$$

where δ_0 is the retardance integrated spatially over the area of the pupil.

A PEM with its fast axis oriented at 0°, sandwiched between two crossed quarter-wave-plates (QWPs), one with its fast axis at −45° and the other at 45° operates as a circular retarder that modulates both Q and U. (A linear retarder would modulate V and either Q or U.) Since circular polarization of sunlight scattered from the Earth is expected to be small, it is not essential to measure the V component in flight. Using the Mueller matrix of an ideal circular retarder [37], a focal plane containing an analyzer at 0° followed by a detector and, in parallel, another analyzer at 45° followed by a detector will obtain two polarization measurements given by

$$I_0 = \frac{1}{2}[I + Q\cos\delta + U\sin\delta], \tag{9}$$

$$I_{45} = \frac{1}{2}[I - Q\sin\delta + U\cos\delta]. \tag{10}$$

Substituting Eq. (8) into Eqs. (9) and (10) and using the Bessel function expansions of the cosine and sine of a sinusoid [38],

$$I_0 = \frac{1}{2}[I + J_0(\delta_0)Q] + \left[\sum_{k=1}^{\infty} J_{2k}(\delta_0)\cos 2k(\omega t - \varphi)\right]Q + \left[\sum_{k=0}^{\infty} J_{2k+1}(\delta_0)\sin(2k+1)(\omega t - \varphi)\right]U, \tag{11}$$

$$I_{45} = \frac{1}{2}[I + J_0(\delta_0)U] + \left[\sum_{k=1}^{\infty} J_{2k}(\delta_0)\cos 2k(\omega t - \varphi)\right]U - \left[\sum_{k=0}^{\infty} J_{2k+1}(\delta_0)\sin(2k+1)(\omega t - \varphi)\right]Q, \tag{12}$$

where J_n is the nth-order Bessel function. Therefore, I_0 is a signal whose unmodulated component is proportional to $I + J_0(\delta_0)Q$, plus a high-frequency component with Q modulated at a frequency of 2ω (and higher even harmonics) and U modulated at ω (and higher odd harmonics) [31,33]. An analogous signal is obtained from the measurement I_{45}. Despite the complexity of the modulation terms, the equations are linear in I, Q, and U.

An innovative approach to recovering the Stokes components from Eqs. (11) and (12) has been demonstrated for solar astronomical polarimetry [33–35,39]. The high-frequency time-varying signals are demodulated by rapidly shifting charges within a CCD between optically unmasked and masked detector lines at a frequency phase-locked to the PEM frequency. Accumulated signals are then read out at the slower frame rate and processed to give the components of the Stokes vector. Synchronous charge shifting, or shuffling, in CCDs has also been used in other astronomical applications [40].

Because our application requires polarimetric measurement in the SWIR as well as in the visible, a complementary metal oxide semiconductor (CMOS) readout architecture is more suitable than a CCD. An approach in which charges are alternately shuttled to different caches designed into the CMOS multiplexer has been described [41]. Construction of such a detector appears to be within reach of CMOS technology. However, since electronic noise can accumulate after a large number of caching operations and given the fact that our application does not require kilohertz caching speeds, we developed a different approach. Equations (11) and (12) show that if the scientific application can afford to integrate the signal over intervals long compared to the tens of kilohertz frequency of the PEM, then the high-frequency terms nearly average to zero and the time-averaged portion of the signals are approximately given by

$$I_0 \approx \frac{1}{2}[I + J_0(\delta_0)Q], \tag{13}$$

$$I_{45} \approx \frac{1}{2}[I + J_0(\delta_0)U]. \tag{14}$$

Aerosol imaging from space is just such an application. In theory, by varying the voltage applied to the PEM it is possible to vary the peak amplitude of the retardance and therefore the value of the coefficient $J_0(\delta_0)$ that multiplies Q and U. Such an approach would permit solving Eqs. (13) and (14) for I, q, and u. However, a PEM is a resonant oscillator with a high mechanical quality factor Q of the order of 10^4, with an inherent time constant equal to $2Q/f$, where f is the PEM resonant frequency. For $Q \sim 10^4$ and $f \sim 42$ kHz, the time constant is ~0.5 s. One would expect this to limit the ability to modulate the peak retardance with low power consumption to about 1 Hz, which is too slow for our application. Laboratory experiments have confirmed this. Using a Hinds Instruments, Inc. II/FS47 octagonal fused-silica PEM system operating at a resonant frequency of 47 kHz, and alternately applying and removing the PEM drive voltage, we found the ring down time to be ~300 ms. Conversely, it took ~400 ms to reach nominal oscillation amplitude (ring up time) after the drive voltage was connected. Thus the high Q was confirmed. If the amplitude is modulated more quickly, the PEM response is damped. This limits the amplitude modulation frequency to ~1 Hz. We demonstrated a reduced ring down time to ~40% of the nominal by replacing the drive signal with a 180° phase shifted drive signal of equal power. With greater power, it should be possible to reduce this further. Similarly, driving with a larger amplitude could shorten the ring up time. Nonetheless, achieving an amplitude modulation that approaches the desired 25 Hz rate is not possible with this approach.

B. Dual Photoelastic Modulators

Given that readout of the resonant frequency-modulated signals from a single PEM is too rapid for our application, and modulation of the amplitude cannot be done rapidly enough, we developed a method using two PEMs in tandem with their retardance axes aligned, oscillating at slightly different frequencies. Assuming for simplicity that the two

PEMs have the same peak retardance δ_0 (see Subsection 4.G), the combined retardance of a dual-PEM system is given by

$$\begin{aligned}\delta(t) &= \delta_0 \sin(\omega_1 t - \varphi_1) + \delta_0 \sin(\omega_2 t - \varphi_2) \\ &= 2\delta_0 \cos(\omega_b t - \eta)\sin(\bar{\omega} t - \bar{\varphi}),\end{aligned} \tag{15}$$

where ω_1 and ω_2 are the resonant frequencies of the two PEMs and φ_1 and φ_2 are the phases of the oscillations relative to an arbitrary time origin. The carrier frequency $\bar{\omega}$ is the average of the two PEM frequencies, and $\bar{\varphi}$ is the average of φ_1 and φ_2. The relatively slow beat frequency ω_b, equal to $(\omega_2 - \omega_1)/2$, modulates this signal. The term η equals $(\varphi_2 - \varphi_1)/2$. As shown in Eq. (6), the resonant frequency of a PEM is inversely proportional to the size of the glass element. Thus, by sizing the two PEMs differently, the beat frequency can be made to be a nearly arbitrary value from a few hertz to a few hundreds of hertz or higher.

We define an image frame to be the time it takes a pushbroom imager to acquire a single line of data, which for MSPI (and MISR) is of the order of 40 ms, during which a spacecraft in low Earth orbit traverses a ground distance of 275 m. In general, the period of the high-frequency carrier wave will not be synchronous with the image frame boundaries. Therefore, if we define $t = 0$ to be the starting time of an arbitrary frame of image data, the phasing of the high-frequency oscillations of the two PEMs will be different from one frame to another. We let φ_0 be the value that the mean phase φ takes at $t = 0$ for that frame. The combined retardance during the frame is given by

$$\delta(t) = z(t)\sin(\bar{\omega} t - \varphi_0), \tag{16}$$

where

$$z(t) = 2\delta_0 \cos(\omega_b t - \eta). \tag{17}$$

Comparison of Eq. (16) with Eq. (8) shows that the expression $z(t)$ takes the place of δ_0 and the terms $\bar{\omega}$, φ_0 replace ω, φ in Eqs. (11) and (12). That is,

$$\begin{aligned}I_0 = \frac{1}{2}[I + J_0[z(t)]Q] + \left[\sum_{k=1}^{\infty} J_{2k}[z(t)]\cos 2k(\bar{\omega} t - \varphi_0)\right]Q \\ + \left[\sum_{k=0}^{\infty} J_{2k+1}[z(t)]\sin(2k+1)(\bar{\omega} t - \varphi_0)\right]U,\end{aligned} \tag{18}$$

$$\begin{aligned}I_{45} = \frac{1}{2}[I + J_0[z(t)]U] + \left[\sum_{k=1}^{\infty} J_{2k}[z(t)]\cos 2k(\bar{\omega} t - \varphi_0)\right]U \\ - \left[\sum_{k=0}^{\infty} J_{2k+1}[z(t)]\sin(2k+1)(\bar{\omega} t - \varphi_0)\right]Q.\end{aligned} \tag{19}$$

Because $\omega_b \ll \bar{\omega}$, integration over subframe sample times long with respect to $\bar{\omega}$ but short compared

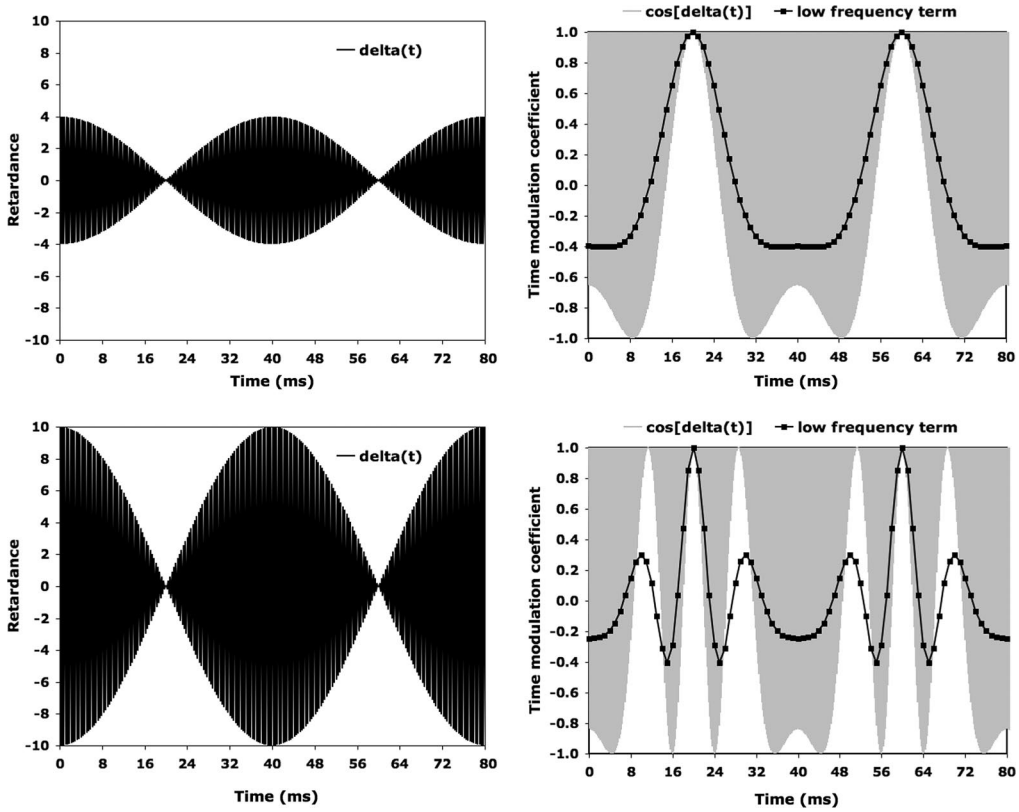

Fig. 1. Combined retardance of two PEMs with a small frequency difference as a function of time (over two 40 ms frame intervals). The right-hand plots show instantaneous cosine of retardance (gray) and the approximate sampled signals obtained by averaging over 1.25 ms intervals (black), thus filtering out the high frequency. The top plots are for $\delta_0 = 2$ and the bottom plots are for $\delta_0 = 5$ rad.

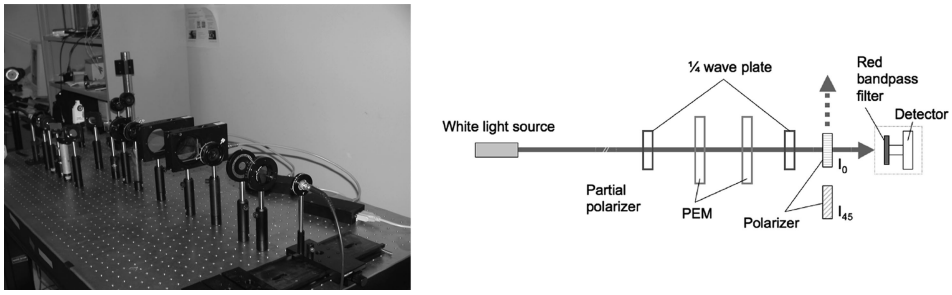

Fig. 2. Left, PEM test setup on an optical bench at JPL. Right, Schematic of the optical system.

to ω_b generates measured signals approximately given by

$$I_0 \approx \frac{1}{2}[I + J_0[2\delta_0 \cos(\omega_b t - \eta)]Q], \tag{20}$$

$$I_{45} \approx \frac{1}{2}[I + J_0[2\delta_0 \cos(\omega_b t - \eta)]U]. \tag{21}$$

A birefringent material having indices of refraction n_e and n_o for the extraordinary and ordinary rays has retardance well approximated by $\delta = 2\pi(n_e - n_o)d/\lambda$, assuming material thickness d and wavelength λ. Operation of the dual-PEM system in multiple spectral bands in the visible and shortwave infrared requires the approach to work over a wide range of δ_0. The shape of the averaged periodic waveform depends on the magnitude of δ_0, and is illustrated in Fig. 1 for $\delta_0 = 2$ and 5 rad. Thus, our broadband polarimeter differs from other dual-PEM concepts that have been optimized for monochromatic operation [39].

To demonstrate this dual-PEM concept, a benchtop polarimeter was constructed as shown in Fig. 2. The polarization state generator is a white light source followed by a tiltable glass plate; this partially polarizes the beam as a function of the plate angle. A rotatable polarization analyzer is used for the detection of Q and U, and is also used as the control measurement of the polarization state. A red filter limits the spectral bandpass. The final element is a photodiode detector. The dual-PEM system consists of Hinds Instruments, Inc. II/IS42 fused-silica PEMs with resonant frequencies near 42 kHz and a beat frequency of 9 Hz. Figure 3 compares the shape of oscilloscope traces of the resulting signal (left) with theoretical predictions (right). The shapes of the curves follow the theory described by Eqs. (20) and (21).

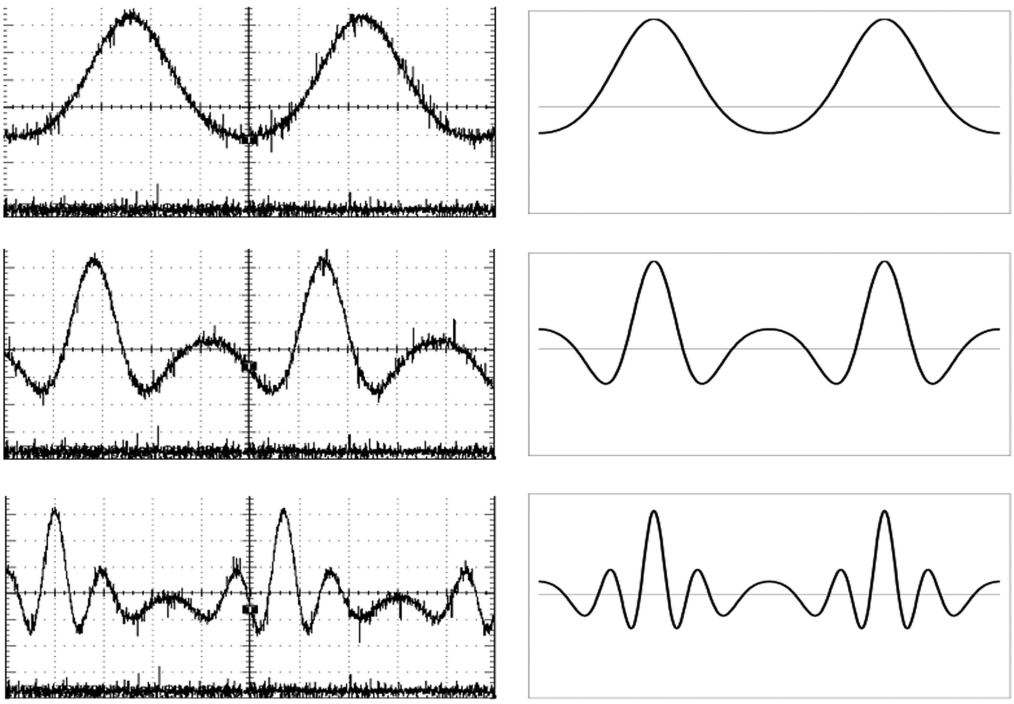

Fig. 3. Oscilloscope traces of measured signal as a function of time (left) compared with theoretical modulation curves (right) for a dual-PEM system as a function of the maximum amplitude in each PEM. From top to bottom, the curves are for a maximum retardance amplitude of 1/4 wave, 1/2 wave, and 1 wave.

4. Achieving the Required DOLP Performance

A. Dual-Photoelastic-Modulator Implementation in a Practical Optical System

The most difficult requirement for MSPI is the 0.5% DOLP tolerance. As noted in Subsection 2.B, all polarimetric measurements require multiple radiometric measurements that are differenced or similarly manipulated to calculate the polarimetric parameters of interest. For a pushbroom imager, adjacent rows of pixels with different analyzers can acquire the necessary measurements. Experience with MISR and other orbiting spectroradiometers has shown that temporal drift of pixel responsivity and calibration errors can cause radiometric uncertainties of 1%–2%, making 0.5% DOLP measurements problematic. The dual-PEM configuration overcomes these limitations by deriving the inputs to DOLP without the need to subtract measurements acquired from different detectors.

A three-mirror reflective off-axis design suitable for implementing the dual-PEM imaging approach is being prototyped. The effective focal length is 29 mm. A ray-trace diagram of the $f/5.6$ optical design is shown in Fig. 4. This system meets the $\pm 31° \times \pm 1°$ FOV requirement discussed in Subsection 2.B. Chief rays from all points in the field are telecentric in image space. The system stop is located between mirror 2 (M2) and mirror 3 (M3). To use the tandem PEMs for the measurement of I, Q, and U (but not V), the system is operated as a circular retardance modulator by adding two QWPs. The first is placed before the PEMs and has its fast axis oriented at $-45°$; the second is placed after the PEMs and has its fast axis oriented at 45°. When a linearly polarized beam is incident on the circular retardance modulator, the polarization of the exiting beam remains linear but its orientation rocks back and forth as the PEMs oscillate. The two PEMs and QWPs are placed on either side of the system stop, thereby minimizing the size of the beam traversing the dual-PEM assembly.

Because MSPI must work over a broad spectral range, the QWPs need to be achromatized. Given that the magnitude of V is expected to be $<0.1\%$ of the intensity, we calculate that the retardance should be within 20% of the ideal value ($\pi/2$) for circular polarization to contribute at most 0.03% error to our 0.5% DOLP error budget. Circular diattenuation, which can occur through the interaction of sequences of linear diattenuations and linear retardances oriented at 45° to each other, is expected to be negligible. Deviations of the alignments of the fast axes of the QWPs and PEMs from their ideal values, along with static retardance errors, will lead to a coupling of q into u and vice versa. As with most polarimeters, errors of this nature can be dealt with through preflight system calibration. Therefore, in the following sections we address errors peculiar to the dual-PEM system, notably those concerned with uncertainty in PEM retardance amplitudes and phases. Measurement noise is addressed in Subsection 4.H.

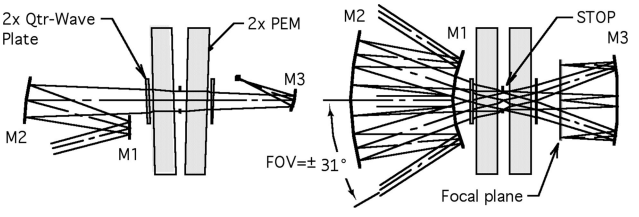

Fig. 4. Side view (left) and top view (right) of a three-mirror camera design with an integrated dual-PEM circular retarder. The PEMs have a small wedge angle between them to minimize ghosting.

B. Signal Integration and Sampling Effects

Equations (20) and (21) assume that the beat signal is constant over multiple cycles of the high-frequency carrier wave. This is the quasi-static approximation. We now derive the more exact form of I_0; a similar result applies to I_{45}. We assume that each term on the right-hand side of Eq. (18) is integrated over multiple cycles of the high-frequency wave, each with period $T = 2\pi/\bar{\omega}$. The integration intervals are centered at sample times denoted $\tilde{t}$, and we allow for the possibility that the integration interval t_{int} is not an exact integer number of cycles by setting the integration interval to $[\tilde{t} - \alpha T/2, \tilde{t} + \alpha T/2]$, where α expresses the integration time as multiples of T. A second-order Taylor expansion is used for the low-frequency term, making use of the formula for the derivative of a Bessel function [38]. A first-order Taylor series is adequate for the high-frequency terms. The resulting expression for the sampled beat signal is

$$
\begin{aligned}
I_0(\tilde{t}) = \frac{1}{2}\big[I + F(\tilde{t})Q\big]
&+ \left[\sum_{k=1}^{\infty} J_{2k}\big[z(\tilde{t})\big]\frac{\sin 2k\pi\alpha}{2k\pi\alpha}\cos 2k\big(\bar{\omega}\tilde{t} - \varphi_0\big)\right]Q \\
&- \left[\frac{\delta_0\omega_b \sin\big(\omega_b\tilde{t} - \eta\big)}{\bar{\omega}}\sum_{k=1}^{\infty} A_k\big[z(\tilde{t})\big]\right. \\
&\times \left.\left[\cos 2k\pi\alpha - \frac{\sin 2k\pi\alpha}{2k\pi\alpha}\right]\sin 2k\big(\bar{\omega}\tilde{t} - \varphi_0\big)\right]Q \\
&+ \left[\sum_{k=0}^{\infty} J_{2k+1}\big[z(\tilde{t})\big]\frac{\sin(2k+1)\pi\alpha}{(2k+1)\pi\alpha}\right. \\
&\times \left.\sin(2k+1)\big(\bar{\omega}\tilde{t} - \varphi_0\big)\right]U \\
&+ \left[\frac{\delta_0\omega_b \sin\big(\omega_b\tilde{t} - \eta\big)}{\bar{\omega}}\sum_{k=0}^{\infty} B_k\big[z(\tilde{t})\big]\right. \\
&\times \left.\left[\cos(2k+1)\pi\alpha - \frac{\sin(2k+1)\pi\alpha}{(2k+1)\pi\alpha}\right]\right. \\
&\times \left.\cos(2k+1)\big(\bar{\omega}\tilde{t} - \varphi_0\big)\right]U, \qquad (22)
\end{aligned}
$$

where

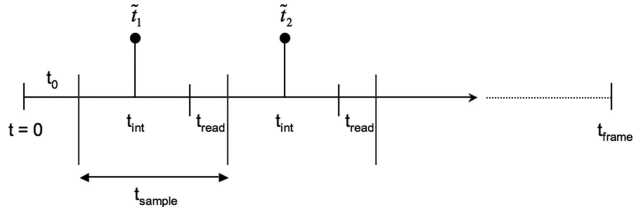

Fig. 5. Timing of sample and integration intervals during a frame.

$$F(\tilde{t}) = J_0[z(\tilde{t})] + \frac{1}{3}\left(\frac{\delta_0 \alpha \pi \omega_b}{\bar{\omega}}\right)^2 \{\cos 2(\omega_b \tilde{t} - \eta) \times J_0[z(\tilde{t})] + J_2[z(\tilde{t})]\}, \quad (23)$$

$$A_k[z(\tilde{t})] = \frac{1}{2k}[J_{2k-1}[z(\tilde{t})] - J_{2k+1}[z(\tilde{t})]], \quad (24)$$

$$B_k[z(\tilde{t})] = \frac{1}{2k+1}[J_{2k}[z(\tilde{t})] - J_{2k+2}[z(\tilde{t})]], \quad (25)$$

and we have made use of the recursion relationship for Bessel functions [38]. We define the time between each measurement, t_{sample}, such that the duration and spacing between each sample is βT. We do not require the entire sample time to be used for integration; that is, we allow $t_{int} < t_{sample}$, or equivalently, $\alpha < \beta$. The remaining time within the sample interval, $t_{read} = t_{sample} - t_{int}$ is used for detector readout. We also permit the beginning of the first integration interval to be offset from the start of the frame by a time delay $t_0 = \gamma T$. The timing diagram is shown in Fig. 5.

The right-hand side of Eq. (22) consists of five terms. The first (low-frequency) term dominates, and takes into account the variation of the low-frequency signal during an integration interval. Figure 6 shows the components of the modulation function $F(\tilde{t})$ for various values of δ_0. In these examples, $\bar{\omega} = 42$ kHz, $\omega_b = 12.5$ Hz, $\alpha = 50$, and $\eta = 0$. This value of the beat frequency corresponds to repetition of the modulation pattern with a frequency of 25 Hz. The value of α is derived from the assumption that over a 40 ms interval, the modulation pattern is sampled 32 times with 1.25 ms duration for each sample. This corresponds to $\beta = 52.5$ for the sample duration, and a few cycle periods are allocated to t_{read}. We find that Q is underestimated by 1%–2% if the second-order term in Eq. (23) is ignored in the system model. Thus, this term must be included in order to meet our 0.5% DOLP tolerance objective. The choice of $N = 32$ allows (a) the modulation pattern to be oversampled, (b) the signal-to-noise ratio (SNR) for each measurement to be dominated by photon shot noise, and (c) the maximum signal during each integration interval to be within the detector full well capacity. A lower bound on N is established by the requirement to resolve the peaks and minima of the modulation patterns illustrated in Fig. 1. For $\delta_0 = 5$ rad, this

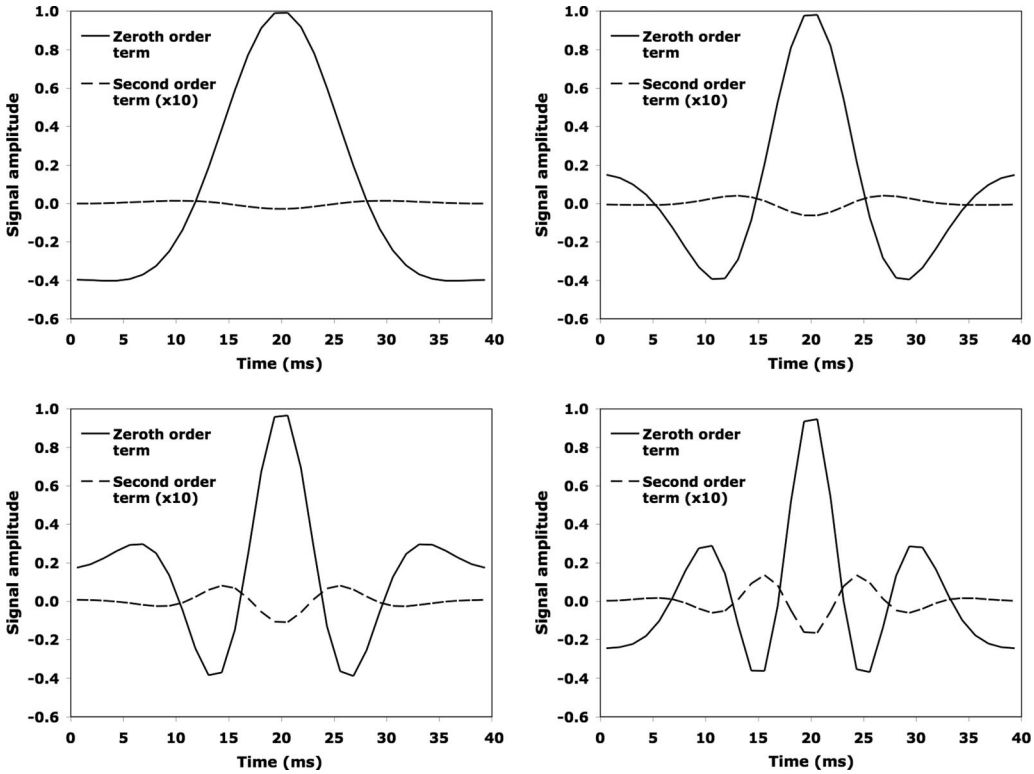

Fig. 6. Relative magnitudes of the low-frequency terms modulating the Stokes components for the set of parameters described in the text. The low-frequency terms are the zeroth- (J_0) and second-order components of the expression $F(\tilde{t})$ in Eq. (23). The second-order term has been multiplied by 10 to make its magnitude and shape more apparent. The four plots are for different values of the peak retardance δ_0: upper left, 2; upper right, 3; lower left, 4; lower right, 5 rad.

minimum N is ~8. However, sensitivity to errors in the knowledge of δ_0 and to measurement noise (see Subsections 4.D and 4.H) increases this value by more than a factor of 2. Substantial margin is obtained with $N = 32$. Provided that N is sufficiently large, the results are not strongly dependent on the exact value of N.

C. Minimization of High-Frequency Signal Residuals

We now examine the conditions under which the high-frequency "noise" terms in Eq. (22) are minimized. It is straightforward to see that terms 2 and 4 are identically zero if α is an integer. Figure 7 shows the effect of changing α on the magnitude of the high-frequency residual terms for δ_0 of 5 rad. To examine the effect of these noise terms on DOLP accuracy, simulated signals were calculated using Eq. (22), and then least-squares analysis was used to solve for q, ignoring the high-frequency terms. An analogous expression to Eq. (22) for $I_{45}(\tilde{t})$ was used to solve for u. To derive a worst-case error, DOLP was set to 1.0 with $q = u = 0.707$, η and φ_0 were allowed to vary between $-\pi$ and π in steps of $\pi/4$ rad, the beat frequency was varied between 12.5 and 13.5 Hz in steps of 0.5 Hz, and the average PEM frequency was varied between 41,990 and 42,000 Hz in steps of 5 Hz. The error in DOLP was typically ~0.10% for $\alpha = 49.0$ or 49.5, and of the order of 0.35% for $\alpha = 49.25$ or 49.75.

We now show that by properly phasing the integration intervals relative to the high-frequency signal, terms 3 and 5 also become zero, effectively eliminating the residual error sources illustrated in Fig. 7. Referring to Fig. 5, the time $\tilde{t}_n$ of the nth sample is

$$\tilde{t}_n = t_0 + \frac{t_{\text{int}}}{2} + (n-1)t_{\text{sample}} = \left[\gamma + \frac{\alpha}{2} + (n-1)\beta\right]T. \tag{26}$$

Using knowledge of the phase φ_0 at the start of the frame, we set the time delay such that $\gamma = (\varphi_0/2\pi) + 1/4$. By requiring β to be either an integer or half integer, then at the start of each integration interval the phase of the high-frequency signal is one-fourth of a cycle after transitioning through zero. Under these conditions,

$$\bar{\omega}\tilde{t}_n - \varphi_0 = \frac{\pi}{2}[1 + 2\alpha + 4(n-1)\beta]. \tag{27}$$

Remembering that α is an integer, the term inside the square brackets in Eq. (27) is an odd integer, with the consequence that $\sin 2k(\bar{\omega}\tilde{t}_n - \varphi_0) = 0$ and $\cos(2k+1)(\bar{\omega}\tilde{t}_n - \varphi_0) = 0$, driving terms 3 and 5 in Eq. (22) to zero, as required. The ability to do this precisely depends on the resolution of the master clock used to drive the electronic circuitry. Numerical experiments suggest that for PEM frequencies in the

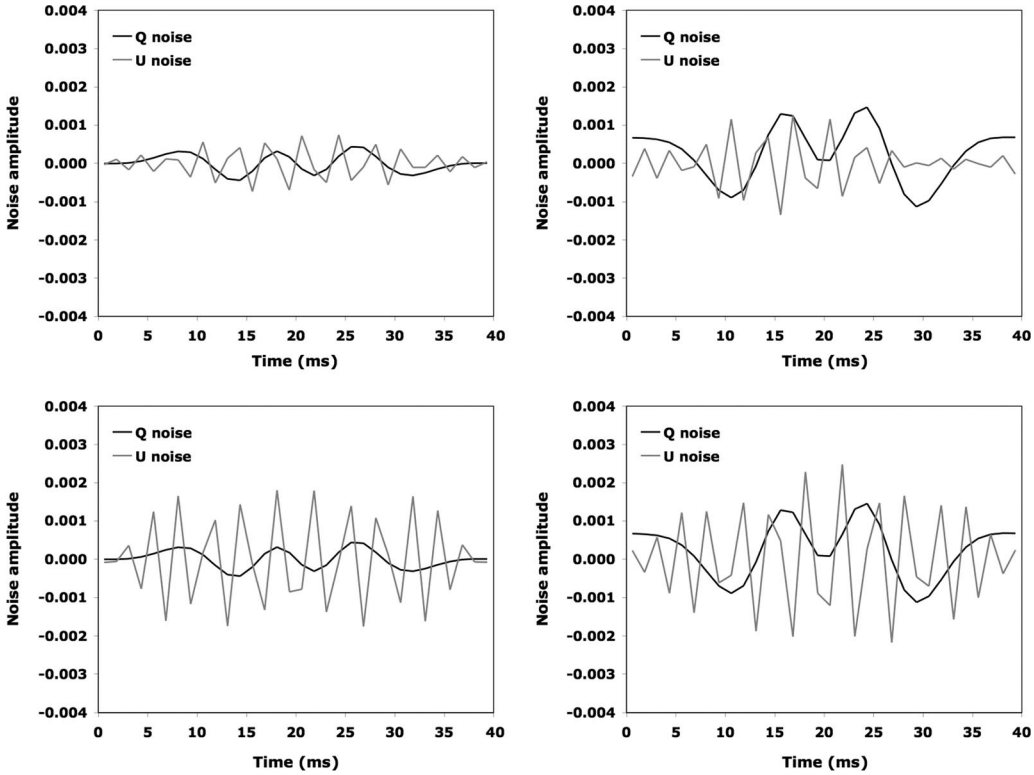

Fig. 7. Curves labeled "Q noise" correspond to the sum of high-frequency residual terms 2 and 3 in Eq. (22) and the curves labeled "U noise" are the sum of terms 4 and 5. The upper left-hand plot is for $\alpha = 49.00$; upper right, $\alpha = 49.25$; lower left, $\alpha = 49.50$; lower right, $\alpha = 49.75$. For these plots, $\delta_0 = 5$ rad and $\varphi_0 = 1$ rad. The other parameters are as in Fig. 6. Note the magnified scale of the y axis.

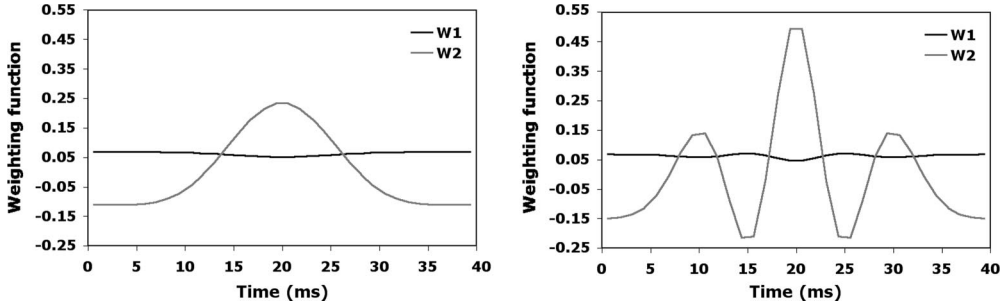

Fig. 8. Weighting functions W_1 and W_2, the first and second rows of the polarimetric data reduction matrix, derived from the two basis functions 0.5 and $0.5J_0$. The left-hand plot is for $\delta_0 = 2$ and the right-hand plot is for $\delta_0 = 5$ rad.

ranges given above, DOLP errors are kept below 0.03% if the clock speed exceeds 20 MHz.

D. Sensitivity of DOLP Retrieval to Errors in Retardance

In Stokes polarimetry, the objective is to determine the Stokes parameters from a series of radiometric measurements. The data reduction is a linear estimation process, and lends itself to efficient solution using linear algebra, usually with a least-squares estimator to find the best match to the data. In MSPI, a vector of radiometric measurements, $\mathbf{I}_0$, acquired by the array with the 0° analyzer, is related to I and Q by the polarimetric measurement matrix, $\mathbf{B}$:

$$\mathbf{I}_0 = \begin{bmatrix} I_{0,1} \\ I_{0,2} \\ \vdots \\ I_{0,N} \end{bmatrix} = \mathbf{B} \cdot \begin{bmatrix} I \\ Q \end{bmatrix} = \frac{1}{2} \begin{bmatrix} 1 & F\left[z(\tilde{t}_1)\right] \\ 1 & F\left[z(\tilde{t}_2)\right] \\ \vdots & \vdots \\ 1 & F\left[z(\tilde{t}_N)\right] \end{bmatrix} \begin{bmatrix} I \\ Q \end{bmatrix}, \tag{28}$$

where the columns of $\mathbf{B}$ describe the time-varying modulation patterns created in the data by each of the Stokes parameters, and are known as the *basis functions.* The rows of $\mathbf{B}$ are known as the *analyzer vectors.* The Stokes parameter estimates $\hat{I}$ and $\hat{Q}$ are calculated from $\mathbf{I}_0$ using a matrix inverse, the *polarimetric data reduction matrix.* In general, the matrix $\mathbf{B}$ is not square and its inverse is not unique. The least-squares estimate is obtained with a particular matrix inverse, the pseudoinverse $\mathbf{W}$:

$$\mathbf{W} = \left(\mathbf{B}^T\mathbf{B}\right)^{-1}\mathbf{B}^T, \tag{29}$$

from which the Stokes vector is determined from a set of linear equations,

$$\begin{bmatrix} \hat{I} \\ \hat{Q} \end{bmatrix} = \mathbf{W} \cdot \mathbf{I}_0. \tag{30}$$

The rows of $\mathbf{W}$ comprise a set of *weighting functions* that generate estimates of the Stokes parameters from weighted sums of the measurements. We let W_1 and W_2 represent the first and second rows, respectively. These functions are illustrated in Fig. 8, where we have approximated the samples of the modulation function F by their dominant, zeroth-order term, $J_0[z(\tilde{t}_n)]$. In actual practice, the complete modulation function would be used.

Construction of the polarimetric data reduction matrix requires accurate estimates of the parameters describing the dual PEM system, namely the retardance δ_0, the phase η, and the beat frequency ω_b. Because ω_b is derived from two resonant oscillators, it will be known very accurately. The estimates of the other two parameters are likely to have some amount of uncertainty or error, leading to systematic errors in the retrieval of q. For example, the left-hand plot in Fig. 9 shows the error in q resulting from a 1% error in δ_0, using the weighting functions shown in Fig. 8.

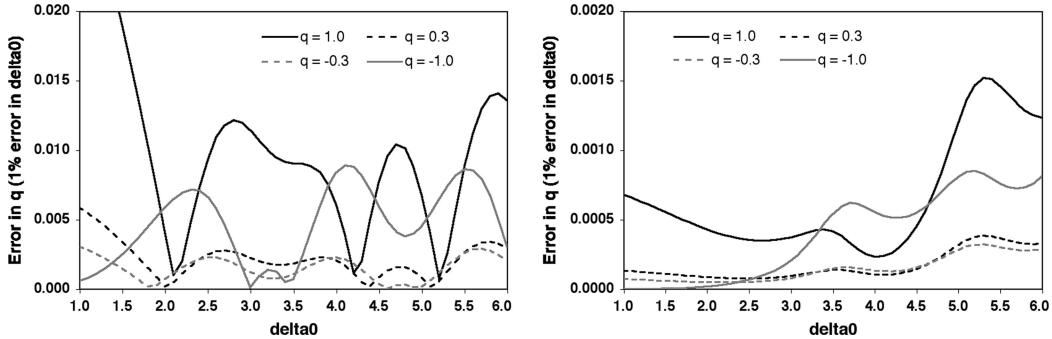

Fig. 9. Left, Error in q resulting from a 1% error in δ_0, as a function of δ_0 and q, using the weighting functions in Fig. 8. Right, Error in q resulting from a 1% error in δ_0, using weighting functions that have been orthogonalized to first-order errors in δ_0 (Fig. 10). Note the change in the y-axis scale by a factor of 10.

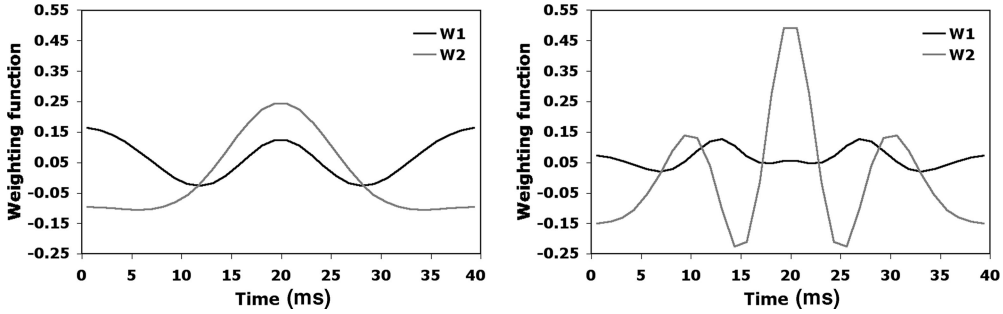

Fig. 10. Weighting functions W_1 and W_2 for $\delta_0 = 2$ (left) and $\delta_0 = 5$ (right) for the case in which the polarimetric data reduction matrix has been orthogonalized to first-order errors in retardance.

Errors increase significantly as the magnitude of q increases, and also are a strong function of the specific value of δ_0. For a given PEM amplitude, retardance is a strong function of wavelength. Thus, the error sensitivity is wavelength dependent. Note that the sensitivity of the I_0 measurement for a positive value of q is the same as the sensitivity of the I_{90} measurement (acquired with an analyzer at 90°) to the corresponding negative value of q. Figure 9 shows that there are regions of relative insensitivity to uncertainty in δ_0. For example, with δ_0 in the range 3.0–3.5, the error in q is $<0.1\%$, provided that q is negative.

Since there is no *a priori* way to guarantee the sign of q, the above discussion suggests that there is benefit in collecting data with both the I_0 and I_{90} arrays. At wavelengths where the error sensitivities of the I_0 and I_{90} arrays are different, the data can be combined to minimize the effect of any error in δ_0. A drawback of this approach is that the I_0 and I_{90} arrays are not optically coregistered, and data resampling is necessary to combine the results. On the other hand, it is possible to overcome the sensitivity of the I_0 measurements to errors in δ_0 by orthogonalizing the weighting functions used in the retrieval of q to first-order errors in PEM retardance. If the assumed retardance, $\hat{\delta}_0$, is close to the true value, δ_0, then

$$I_0 = \frac{1}{2}[I + F(z)Q] \approx \frac{1}{2}\left[I + F(\hat{z})Q + \left.\frac{\partial F}{\partial \delta_0}\right|_{z=\hat{z}} (\delta_0 - \hat{\delta}_0)Q\right], \tag{31}$$

where $\hat{z}$ is calculated using $\hat{\delta}_0$. We can therefore modify Eq. (28) by adding a third basis function. In this three-parameter formulation, the first two rows of the new pseudoinverse $\mathbf{W}$, i.e., the weighting functions W_1 and W_2, are both orthogonal to the third basis function, rendering the resulting estimates of I and Q insensitive to first-order errors in retardance. These new weighting functions are shown in Fig. 10 for $\delta_0 = 2$ (left) and 5 (right), again assuming for purposes of illustration that F is approximated by $J_0(z)$, such that

$$I_0 \approx \frac{1}{2}\left[I + J_0(\hat{z})Q - \hat{z}J_0(\hat{z})\frac{(\delta_0 - \hat{\delta}_0)}{\hat{\delta}_0} Q\right]. \tag{32}$$

Using these weighting functions to retrieve q results in the sensitivity to errors in δ_0 shown on the right-hand side of Fig. 9. Relative to the two-parameter formulation, the errors in q for a 1% error in δ_0 have been reduced by about an order of magnitude, and are $\sim 0.15\%$ in the worst case ($q = 1$) and more typically, substantially lower.

In practice, the estimate $\hat{\delta}_0$ can be obtained from an optical probe that passes a polarized beam generated by a LED and a linear polarizer through a portion of the dual-PEM assembly outside the area used for imaging. Since retardance varies spatially across the PEMs as shown in Eq. (7), preflight calibration will be necessary to translate the retardance at the location of the probe beam to the value within the imaging aperture, as well as to the relevant wavelength. Because this calibration will not be perfect, orthogonalizing the weighting functions to first-order errors in δ_0 permits approximately a factor of 10 relaxation in the allowable uncertainty in $\hat{\delta}_0$. For completeness, we must examine the performance of these estimators in the presence of measurement noise. This topic is explored in Subsection 4.H. We also note that the orthogonalization process yields a weighting function, W_3 (the third row of the polarimetric data reduction matrix), which can be used to estimate the parameter $(\delta_0 - \hat{\delta}_0)Q$. Since the weighting function W_2 provides an estimate of Q, the ratio of these parameters gives an estimate of the retardance error. Because this is a static, scene-independent value, data from many measurements can be combined together to retrieve it, allowing the estimate of PEM retardance amplitude to be improved.

E. Effect of Finite Spectral Bandwidth

Obtaining adequate SNR requires the measurements to be acquired over some finite bandwidth. If the retardance at some reference wavelength λ_r is denoted δ_{0r}, then at any wavelength $\delta_0 \approx \delta_{0r}\lambda_r/\lambda$. To illustrate the effects of integrating the modulation function over wavelength, we assume that I and Q are invariant over the spectral interval, and approximate the modulation by the J_0 Bessel function. The average value over a finite spectral bandpass (assumed to have uniform response with wavelength) is given by

$$\bar{J}_0 = \frac{1}{\bar{\lambda}\Delta\lambda}\int_{\lambda_1}^{\lambda_2} J_0[2\delta_{0r}\lambda_r \cos(\omega_b t - \eta)/\lambda]\lambda d\lambda, \quad (33)$$

where the additional multiplication by λ is included in the integrand because the photodetectors respond to photon flux, thus the conversion takes into account the number of photons per unit of energy. We also have let $\bar{\lambda} = (\lambda_1 + \lambda_2)/2$ and $\Delta\lambda = \lambda_2 - \lambda_1$. Equation (33) can be evaluated analytically by expanding J_0 in a first-order Taylor series in wavelength, from which we derive

$$\bar{J}_0 = J_0(z) + \frac{1}{12}\left(\frac{\Delta\lambda}{\bar{\lambda}}\right)^2 z J_1(z), \quad (34)$$

where z is defined at the band center. Comparison of Eqs. (32) and (34) shows that finite spectral bandwidth acts like an offset in the retardance. Because the terms resulting from a retardance error and a finite spectral bandwidth have the same functional form, orthogonalizing the retrieval basis functions as discussed in the previous section desensitizes the retrievals to this effect.

F. Effects of Phase Errors and Scene Gradients

We anticipate difficulty controlling the beat frequency precisely over a long-duration satellite mission, and long-term drifts in the PEM resonant frequencies will also make it difficult to control the phase φ_0. Indeed, high-frequency phase stability of a dual-PEM system has been extremely difficult to achieve in practice [42], making such approaches problematic when demodulation of the waveform at the resonant frequencies is required. However, our approach requires phase *knowledge*, not phase *stability*. As shown in Subsection 4.C, synchronization of the sample integration windows to the carrier wave is needed to minimize high-frequency noise. In this section, we derive the requirement on knowledge of the beat signal phase in order to solve accurately for q and u. Because phase does not vary spatially over the extent of a PEM, the optical probe mentioned in the previous section can be used to provide a direct measurement. We anticipate that the timing of the peak of the modulation function can be determined to within one high-frequency cycle period using a phase-locked loop. Since a variation in η from $-\pi/2$ to $+\pi/2$ moves the peak of the modulation function from the beginning to the end of a 40 ms frame, the duration of 1 cycle of a 42 kHz wave, or $\sim$24 μs, corresponds to an error of 0.002 rad. In the absence of any gradients in I and Q, the resulting error in the data reduction weighting functions causes an error in the retrieved value of q that is quadratic in the phase error and increases roughly linearly with δ_0, reaching a value of $\sim$0.0002 for $\delta_0 = 6$ when $q = 1$ or -1. This negligible error decreases proportionately as the magnitude of q decreases.

A more realistic scene model includes gradients in I, Q, and U, because the target area imaged by a given pixel moves during a frame due to spacecraft motion. Any spatial variation in the scene translates into a temporal variation in the recorded signal, in addition to that introduced by the PEM modulation. This introduces an additional source of error. By synchronizing the frame time to the beat frequency, however, it is possible to center the modulation functions within each frame. Since the modulation functions are symmetric, this has the advantage of making the polarization retrievals insensitive to linear gradients—as well as any other odd function of time—because the weighting functions are even and therefore orthogonal to these scene variations. In practice, however, this centering will not be perfect. To explore the sensitivity to phase errors in the presence of gradients, we recall that the distance moved in one sample time ($\sim$1.25 ms) is $\sim$8 m for a spacecraft in low Earth orbit. With a ground footprint size of $\sim$275 m, high-frequency spatial variations will be washed out. Thus, a scene model with linear gradients seems reasonable, and can be modeled during the course of a frame as

$$I = \bar{I}(1 + c_I\tau), \quad (35)$$

$$Q = \bar{I}(q + c_Q\tau), \quad (36)$$

where $q = \bar{Q}/\bar{I}$, $\bar{I}$ and $\bar{Q}$ are the frame-averaged values, c_I and c_Q parameterize the magnitude of linear gradients in I and Q as fractions of the mean intensity $\bar{I}$, and the dimensionless time parameter τ is defined as

$$\tau = \left[\tilde{t} - \bar{\tilde{t}}\right]\Big/\left[\tilde{t}_N - \tilde{t}_1\right]. \quad (37)$$

The overbar indicates the average over a frame, and the denominator is the time difference between the first and last sample. The parameter τ varies linearly from -0.5 to $+0.5$ and has zero mean.

Figure 11 (left) shows the retrieval error in q as a function of δ_0 for $q = 0.5$ and various values of c_I and c_Q. The modulation signal has a phase offset of 0.002 rad, and there is an additional phase knowledge error of 0.002 rad (i.e., equivalent to an error of one high-frequency cycle in each case). With $c_I = 0.5$ and $c_Q = 1.0$, q varies from 0.0 to 0.8 across the frame, and with $c_I = 0.0$, q varies from 0.0 to 1.0. The resulting errors in q can exceed 0.001; however, the modeled gradients are probably larger than are expected in practice, and the errors will decrease with smaller q. Furthermore, we can eliminate the dominant source of error by orthogonalizing the weighting functions against linear gradients in I and Q. This is accomplished by adding τ and $\tau J_0[z(\tilde{t})]$ to the set of basis functions. As long as the phase offsets are small, the weighting functions W_1 and W_2 change only slightly. (In the examples shown in this section, the weighting functions have already been orthogo-

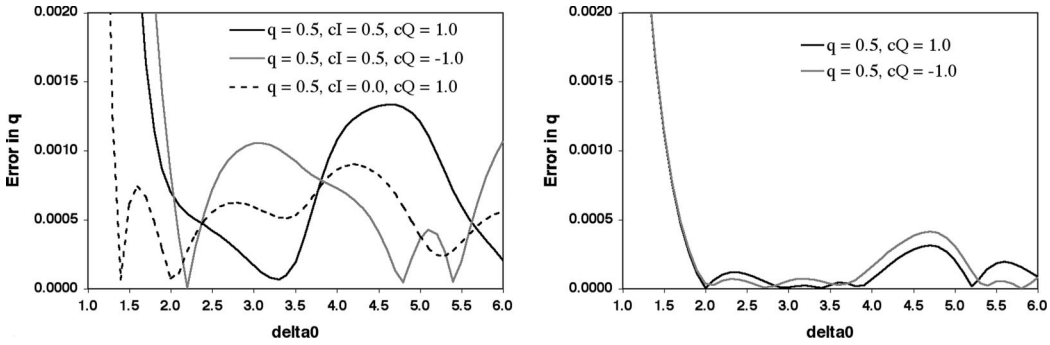

Fig. 11. Left, Retrieval error in q as a function of δ_0 for $q = 0.5$ and various values of the scene gradient coefficients. The modulation signal has a phase offset of 0.002 rad, and a phase knowledge error of 0.002 rad. Right, Retrieval error in q for the same parameter values but using weighting functions that have been orthogonalized against linear gradients in I and Q. In this case there is no dependence on the magnitude of the intensity gradient, and the Q gradient introduces an error only because of the phase error.

nalized against errors in δ_0, as described in Subsection 4.D.) Figure 11 (right) shows that the retrieval error in q decreases significantly when this is done, provided that δ_0 exceeds ~1.7. This approach eliminates any dependence on the magnitude of the linear intensity gradient, and the Q gradient introduces an error only because the phase error results in the use of an erroneous weighting function in the data reduction. Even for the large magnitude linear gradients assumed in this illustration, retrieval error in q is reduced to less than 0.0005.

G. Retardance Amplitude Mismatch between the Dual Photoelastic Modulators

The above discussion incorporated the simplifying assumption that the retardance amplitude of each PEM is identical. As noted in Subsection 4.A, the optical system results in slightly different effective retardance for each PEM. Other factors, notably electrical drive strength, could also cause the two PEMs to have different retardance amplitudes. We now generalize the discussion to take this into account, by modifying Eq. (15) as follows:

$$\begin{aligned}\delta(t) &= \delta_1 \sin(\omega_1 t - \varphi_1) + \delta_2 \sin(\omega_2 t - \varphi_2),\\ &= 2\delta_0 \cos(\omega_b t - \eta)\sin(\bar{\omega} t - \bar{\varphi})\\ &\quad + 2\Delta \sin(\omega_b t - \eta)\cos(\bar{\omega} t - \bar{\varphi}),\end{aligned} \tag{38}$$

where δ_1 and δ_2 are the retardance amplitudes of the two PEMs, respectively; $\delta_0 = (\delta_1 + \delta_2)/2$; and $\Delta = (\delta_2 - \delta_1)/2$. Again letting φ_0 be the value that the mean phase $\bar{\varphi}$ at the start of an image frame:

$$\delta(t) = z'(t)\sin[\bar{\omega} t - \varphi_0 + \zeta(t)], \tag{39}$$

where

$$\tan \zeta(t) = (\Delta/\delta_0)\tan(\omega_b t - \eta), \tag{40}$$

$$\begin{aligned}z'(t) = 2\ \mathrm{sgn}[z(t)]\big[&\delta_0{}^2 \cos^2(\omega_b t - \eta)\\ &+ \Delta^2 \sin^2(\omega_b t - \eta)\big]^{1/2}.\end{aligned} \tag{41}$$

The sgn term in Eq. (41) ensures that z' has the proper sign. Equation (39) puts the total retardance into a similar form as Eq. (16), resulting in a modified form of Eq. (18):

$$\begin{aligned}I_0 = \frac{1}{2}[I + J_0[z'(t)]Q] &+ \left[\sum_{k=1}^{\infty} c_{2k}(t)\cos 2k(\bar{\omega} t - \varphi_0)\right]Q\\ &- \left[\sum_{k=1}^{\infty} s_{2k}(t)\sin 2k(\bar{\omega} t - \varphi_0)\right]Q\\ &+ \left[\sum_{k=0}^{\infty} c_{2k+1}(t)\sin(2k+1)(\bar{\omega} t - \varphi_0)\right]U\\ &+ \left[\sum_{k=0}^{\infty} s_{2k+1}(t)\cos(2k+1)(\bar{\omega} t - \varphi_0)\right]U,\end{aligned} \tag{42}$$

where

$$c_n(t) = J_n[z'(t)]\cos n\zeta(t), \tag{43}$$

$$s_n(t) = J_n[z'(t)]\sin n\zeta(t). \tag{44}$$

The functions c_n and s_n depend only on the beat frequency. Using a similar methodology as above to integrate over time windows of duration αT, we find that mismatch in retardance between the two PEMs results in negligible high-frequency contribution.

For small Δ, analytic integration of the low-frequency term in Eq. (42) results in a modified form of the modulation function:

$$F'(\tilde{t}) \approx F(\tilde{t}) - 2\,\frac{J_1[z(\tilde{t})]}{z(\tilde{t})}\,\Delta^2 \sin^2(\omega_b \tilde{t} - \eta), \tag{45}$$

where $F(\tilde{t})$ is from Eq. (23). The correction term for Δ is referred to as the PEM amplitude mismatch term. Unfortunately, the shape of this term closely matches that of the zeroth-order (J_0) function, particularly at low values of δ_0, so we cannot simply orthogonalize against it. An unmodeled mismatch masquerades as a reduced value of Q. Because Δ enters quadratically into Eq. (45), an uncompensated amplitude mismatch of 0.1 leads to approximately a 1% underestimation of Q. Either the mismatch must be included in the data processing model, or it must be reduced to a value

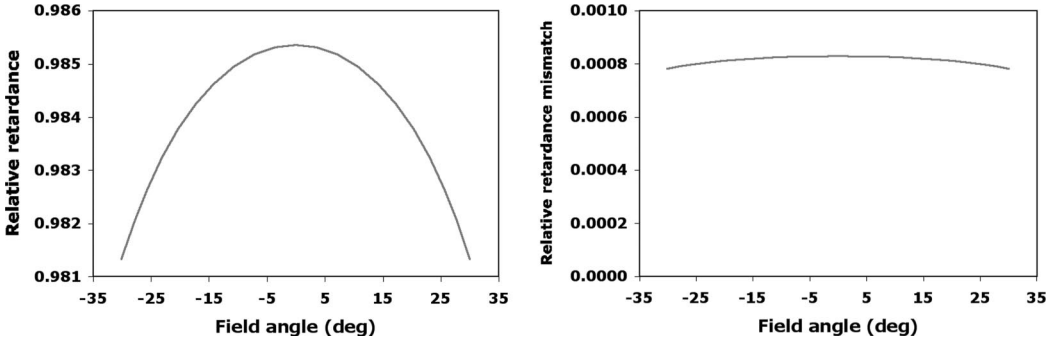

Fig. 12. Left, Relative variation in retardance across the FOV in the cross-track direction, for a system with the exact on axis ray having a retardance of 1.0 rad. Right, Relative retardance mismatch Δ between the two PEMs.

<0.03 so as to contribute no more than a 0.1% error to the DOLP retrieval.

Making use of the optical design described in Subsection 4.A, we now evaluate the variation of δ_0 across the camera FOV and the expected magnitude of Δ. The proximity of the PEMs to the system stop confines the rays to the central regions of each PEM. Along with the high degree of collimation, this helps to ensure that all rays passing through the PEMs receive very close to the same amplitude of retardance modulation. Light is incident on the PEMs at angles ranging from 0° to 21°, resulting in a variation of retardance across the FOV. In addition, because the beam is converging between M2 and M3, there is a small mismatch in the spatially averaged retardance between the two PEMs. To explore these effects, bundles of 81 rays were propagated for a set of locations within the FOV. Assuming that the on-axis ray sees a retardance of unity, the retardance for each ray was obtained by numerical integration along its path through the two PEMs, accounting for spatial variations described by Eq. (7) and path-angle effects. The increase in path length with angle is offset by the decrease in the projection of the path on the stress vector in the plane of the PEM. Weighted averages of the results for the 81 rays were calculated, taking into account the area within the pupil represented by each ray.

The relative retardance amplitude as a function of cross-track location in the $\pm 31°$ FOV is shown in Fig. 12 (left) for a paraxial retardance of 1 rad. The finite bundle size reduces the average retardance by less than 1.5% at the center of the FOV and less than 2% at the edges. Because these effects are fixed, the 0.4% variation across the FOV can be calibrated and accounted for in generating the basis functions for each pixel. The variation in retardance in along-track ($\pm 1°$) dimension of the FOV is negligible.

A plot of the relative retardance mismatch between the two PEMs is shown in Fig. 12 (right). Due to beam convergence, Δ is slightly positive, with a negligible variation with field angle. For an on-axis retardance of 5.0 rad, for example, $|\Delta| < 0.004$ rad. Equation (45) shows that errors in DOLP are proportional to Δ^2, implying that the degree of mismatch that could affect DOLP accuracy is not determined by the optical system, but rather by the accuracy with which the two PEMs can be controlled to have the same retardance. This can readily be done since the retardance amplitude of each PEM is individually controllable.

H. Sensitivity to Measurement Noise

We now generalize the above discussion by supposing that each sample measurement I_{0n} has a noise value ε_n added to it. The estimates $\hat{I}$ and $\hat{Q}$ have associated errors given by

$$\begin{bmatrix} \Delta\hat{I} \\ \Delta\hat{Q} \end{bmatrix} = \mathbf{W} \cdot \boldsymbol{\varepsilon}. \tag{46}$$

For a given set of measurements, the error in q is therefore

$$\Delta q = \frac{\Delta\hat{Q} - q\Delta\hat{I}}{I} = \frac{\sum_{n=1}^{N} (W_{2,n} - qW_{1,n})\varepsilon_n}{I}. \tag{47}$$

Making the simplifying assumption that the noise in each measurement has constant variance ε^2 dominated by photon shot noise on the mean signal (approximately equal to $I/2$), the statistical variance in q is

$$\mathrm{var}(q) = \frac{\varepsilon^2}{I^2}\left[\sum_{n=1}^{N} (W_{2,n} - qW_{1,n})^2\right]. \tag{48}$$

In addition to detector arrays with analyzers at 0° and 45°, the MSPI design for each polarimetric band includes an array with no analyzer. We define SNR to be the signal-to-noise ratio in I for one frame of data acquired by the nonpolarimetric detector. The SNR of each individual measurement is equal to $I^{1/2}$ for a shot noise limited system with I expressed in photon counts, so for N such measurements, $\mathrm{SNR} = (NI)^{1/2}$. The statistical uncertainty in the estimate of q due to noise is therefore equal to

$$unc(q) = \frac{\left[\frac{N}{2}\sum_{n=1}^{N} (W_{2,n} - qW_{1,n})^2\right]^{1/2}}{\mathrm{SNR}} = \frac{s}{\mathrm{SNR}}. \tag{49}$$

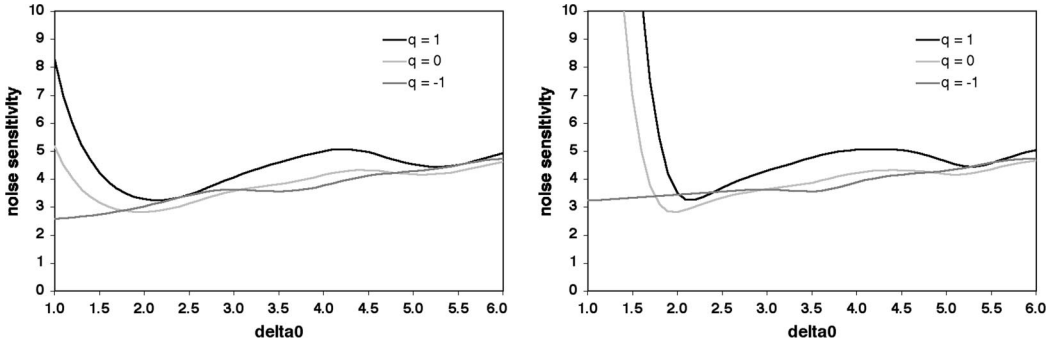

Fig. 13. Left, Solid curves are the "noise sensitivity" factor s for the case where the retrieval weighting functions W_1 and W_2 are as in Fig. 8, under the simplifying assumption that noise variance is constant during a frame and dominated by photon shot noise. Right, Similar to the left-hand plot except that the weighting functions for the retrieval q are the orthogonalized forms of W_1 and W_2, as in Fig. 10.

The parameter s expresses the uncertainty in q as a multiple of the inverse of the SNR of a pure intensity measurement, and thus can be thought of as a "noise sensitivity" factor. Plots of this quantity as a function of δ_0 are shown in Fig. 13. The left-hand plot assumes the weighting functions are as defined in Fig. 8, and the right-hand plot uses the weighting functions that have been orthogonalized against first-order errors in δ_0, as in Fig. 10. Very similar results are obtained when the weighting functions have also been orthogonalized against linear gradients, as long as the phase errors are small. Figure 13 shows that for $\delta_0 \geq 2$ there is very little noise penalty resulting from orthogonalization of the weighting functions. With a typical value $s \sim 4$, a SNR of 1000 causes an uncertainty in q due to shot noise of $\sim$0.004.

5. Summary and Conclusions

This paper introduces a novel concept for spectropolarimetric imaging with high accuracy across a wide field of view. The approach makes use of a circular retardance modulator containing two PEMs with slightly different resonant frequencies to generate a beat signal that modulates the Q and U polarized components of the incident light. The concept can be adapted to applications where the frame rate is in the few to hundreds of hertz range. Imaging over a broad spectral range and with high accuracy in DOLP are key performance requirements for the aerosol remote sensing application that motivates the approach. Many factors, including the performance of mirror coatings, antireflection coatings, polarization analyzers, and control of scattered light are essential to meeting the challenge of 0.5% tolerance in DOLP for a spaceborne imaging polarimeter. This paper concentrates on nonstatic error sources that are unique to this dual-PEM system (see Table 2). We have focused on errors in the relative Stokes parameter q. Making the reasonable assumption that σ_q, the root-mean-squared (rms) error in q is roughly equal to σ_u, the rms error in u, then error propagation shows that the rms error in DOLP $\approx \sigma_q$.

The errors in Table 2 have been calculated assuming high values of $|q|$, and will in practice be smaller since the PEM retardance and phase errors are roughly proportional to q. Table 2 shows that after measurement noise, the next most significant errors result from uncertainties in average PEM retardance and the mismatch in retardance between the two PEMs. This indicates the need for a system within the camera to monitor the PEM retardance amplitudes accurately. Using the fact that spatial variation in retardance across the PEM elements can be measured, an optical probe can be constructed to make use of a portion of the PEM elements outside the central area used for Earth imaging. As noted earlier, a probe consisting of an LED, a set of linear polarizers, and a photodetector can meet this objective.

As with MISR, which acquires multiangle images by employing a set of cameras pointed at discrete angles, the camera approach described in this paper forms the fundamental "building block" for a full, multiangle MSPI instrument. The pointing angles are envisioned to be similar to the MISR suite, and discrete spectral bands for aerosol studies range from 355 to 1610 nm, as indicated in Table 1. (A band near 2130 nm is under investigation.) Intensity imaging

Table 2. Requirements on the Dual-PEM System

Error Source (Section Discussed)	Requirement	Contribution to DOLP Error Budget (%)
Residual high-frequency terms (Subsection 4.C)	Proper phasing of integration intervals; clock speed > 20 MHz	0.03
Retardance amplitude knowledge (Subsection 4.D)	1%	0.15
Phase control and knowledge (Subsection 4.E)	0.002 rad	0.05
Retardance amplitude mismatch between the PEMs (Subsection 4.G)	0.03 rad	0.1
Measurement noise (Subsection 4.H)	SNR $\geq$ 1000	0.4
Root-sum-square		0.44

would be acquired in all channels, which places strict requirements on allowable camera diattenuation in order to meet an absolute radiometric uncertainty requirement of ±3% (similar to MISR). The subset of bands for which polarimetry would be acquired is the subject of ongoing study, and results from NASA's Glory mission later this decade, carrying the APS sensor, will provide valuable insights in this regard. At present, one polarization band in the blue, one in the red, and one in the SWIR are envisioned.

To the best of our knowledge, PEMs have not flown in space, and ruggedization and space qualification of the PEM mounting scheme is an essential element of a viable instrument concept. Current work in partnership with Hinds Instruments, Inc. under NASA sponsorship is tackling this task. The novel concept analyzed in this paper is applicable not only to high-accuracy remote sensing of aerosols but potentially to a host of other scientific endeavors.

We thank Yu Wang for suggesting the novel dual-PEM approach and for performing the initial concept verification experiments, and appreciate helpful discussions with Thomas Cunningham. We thank Neil Beaudry for insightful theoretical analyses, and Karlton Crabtree for performing PEM amplitude modulation experiments using a single PEM. Jet Propulsion Laboratory (JPL) internal Research and Technology Development and NASA Instrument Incubator Program support are gratefully acknowledged. This research is being carried out at the JPL, California Institute of Technology under contract with NASA; at the University of Arizona College of Optical Sciences under subcontract with JPL; and at the Goddard Institute for Space Studies.

References

1. H. Yu, Y. J. Kaufman, M. Chin, G. Feingold, L. A. Remer, T. L. Anderson, Y. Balkanski, N. Bellouin, O. Boucher, S. Christopher, P. DeCola, R. Kahn, D. Koch, N. Loeb, M. S. Reddy, M. Schulz, T. Takemura, and M. Zhou, "A review of measurement-based assessments of the aerosol direct radiative effect and forcing," Atmos. Chem. Phys. **6,** 613–666 (2006).
2. L. A. Remer, D. Tanré, Y. J. Kaufman, C. Ichoku, S. Mattoo, R. Levy, D. A. Chu, B. N. Holben, O. Dubovik, A. Smirnov, J. V. Martins, R. R. Li, and Z. Ahmad, "Validation of MODIS aerosol retrieval over ocean," Geophys. Res. Lett. **29,** 1–4 (2002).
3. D. A. Chu, Y. J. Kaufman, C. Ichoku, L. A. Remer, D. Tanré, and B. N. Holben, "Validation of MODIS aerosol optical depth retrieval over land," Geophys. Res. Lett. **29,** 5–8 (2002).
4. O. Torres, P. K. Bhartia, J. R. Herman, A. Syniuk, P. Ginoux, and B. Holben, "A long term record of aerosol optical depth from TOMS observations and comparison to AERONET measurements," J. Atmos. Sci. **59,** 398–413 (2002).
5. O. Torres, R. Decae, P. Veefkind, and G. de Leeuw, "OMI aerosol retrieval algorithm," in *OMI Algorithm Theoretical Basis Document: Clouds, Aerosols, and Surface UV Irradiance,* P. Stammes and R. Noordhoek, eds. (NASA, 2002), Vol. III, pp. 46–71.
6. J. P. Veefkind, G. de Leeuw, and P. A. Durkee, "Retrieval of aerosol optical depth over land using two-angle view satellite radiometry during TARFOX," Geophys. Res. Lett. **25,** 3135–3138 (1998).
7. P. R. J. North, S. A. Briggs, S. E. Plummer, and J. J. Settle, "Retrieval of land surface bidirectional reflectance and aerosol opacity from ATSR-2 multi-angle imagery," IEEE Trans. Geosci. Remote Sens. **37,** 526–537 (1999).
8. J. V. Martonchik, D. J. Diner, K. A. Crean, and M. A. Bull, "Regional aerosol retrieval results from MISR," IEEE Trans. Geosci. Remote Sens. **40,** 1520–1531 (2002).
9. R. A. Kahn, B. J. Gaitley, J. V. Martonchik, D. J. Diner, K. A. Crean, and B. Holben, "Multiangle Imaging Spectroradiometer (MISR) global aerosol optical depth validation based on 2 years of coincident Aerosol Robotic Network (AERONET) observations," J. Geophys. Res. **110,** D10S04 (2005).
10. R. Kahn, P. Banerjee, and D. McDonald, "The sensitivity of multiangle imaging to natural mixtures of aerosols over ocean," J. Geophys. Res. **106,** 18219–18238 (2001).
11. O. Kalashnikova, R. Kahn, I. N. Sokolik, and W.-H. Li, "Ability of multiangle remote sensing observations to identify and distinguish mineral dust types: optical models and retrievals of optically thick plumes," J. Geophys. Res. **110,** 18S14 (2005).
12. R. Kahn, W.-H. Li, C. Moroney, D. J. Diner, J. V. Martonchik, and E. Fishbein, "Aerosol source characterization from space-based multi-angle imaging," J. Geophys. Res. **112,** D11205 (2007).
13. J. Chowdhary, B. Cairns, M. Mishchenko, and L. Travis, "Retrieval of aerosol properties over the ocean using multispectral and multiangle photopolarimetric measurements from the Research Scanning Polarimeter," Geophys. Res. Lett. **28,** 243–246 (2001).
14. J. Chowdhary, B. Cairns, and L. D. Travis, "Case studies of aerosol retrievals over the ocean from multiangle, multispectral photopolarimetric remote sensing data," J. Atmos. Sci. **59,** 383–397 (2002).
15. M. I. Mishchenko and L. D. Travis, "Satellite retrieval of aerosol properties over the ocean using polarization as well as intensity of reflected sunlight," J. Geophys. Res. **102,** 16989–17014 (1997).
16. J. L. Deuzé, P. Goloub, M. Herman, A. Marchand, G. Perry, S. Susana, and D. Tanré, "Estimate of the aerosol properties over the ocean with POLDER," J. Geophys. Res. **105,** 15329–15346 (2000).
17. O. Hagolle, P. Goloub, P. Y. Deschamps, H. Cosnefroy, X. Briottet, T. Bailleul, J. M. Nicolas, F. Parol, B. Lafrance, and M. Herman, "Results of POLDER in-flight calibration," IEEE Trans. Geosci. Remote Sens. **37,** 1550–1566 (1999).
18. M. I. Mishchenko, B. Cairns, G. Kopp, C. F. Schueller, B. A. Fafaul, J. E. Hansen, R. J. Hooker, T. Itchkawich, H. B. Maring, and L. D. Travis, "Precise and accurate monitoring of terrestrial aerosols and total solar irradiance: introducing the Glory mission," Bull. Am. Meteorol. Soc. **88,** 677–691 (2007).
19. O. P. Hasekamp and J. Landgraf, "Retrieval of aerosol properties over land surfaces: capabilities of multiple-viewing-angle intensity and polarization measurements," Appl. Opt. **46,** 3332–3344 (2007).
20. National Research Council, Committee on Earth Science and Applications from Space, *Earth Science and Applications from Space: National Imperatives for the Next Decade and Beyond* (The National Academies Press, 2007).
21. D. J. Diner, J. C. Beckert, T. H. Reilly, C. J. Bruegge, J. E. Conel, R. A. Kahn, J. V. Martonchik, T. P. Ackerman, R. Davies, S. A. W. Gerstl, H. R. Gordon, J.-P. Muller, R. B. Myneni, P. J. Sellers, B. Pinty, and M. Verstraete, "Multi-angle Imaging SpectroRadiometer (MISR) instrument description and experiment overview," IEEE Trans. Geosci. Remote Sens. **36,** 1072–1087 (1998).
22. V. M. Jovanovic, M. A. Bull, M. M. Smyth, and J. Zong, "MISR in-flight camera geometric model calibration and georectification performance," IEEE Trans. Geosci. Remote Sens. **40,** 1512–1519 (2002).
23. J. S. Tyo, D. L. Goldstein, D. B. Chenault, and J. A. Shaw,

"Review of passive imaging polarimetry for remote sensing applications," Appl. Opt. **45,** 5453–5469 (2006).
24. M. Descour and E. Dereniak, "Computed-tomography imaging spectrometer: experimental calibration and reconstruction results," Appl. Opt. **34,** 4817–4826 (1995).
25. A. M. Locke, D. S. Sabatke, E. L. Dereniak, M. R. Descour, J. P. Garcia, T. K. Hamilton, and R. W. McMillan, "Snapshot imaging spectropolarimeter," Proc. SPIE **4481,** 64–72 (2002).
26. J. S. Van Delden, "Ortho-Babinet polarization-interrogating filter: an interferometric approach to polarization measurement," Opt. Lett. **28,** 1173–1175 (2003).
27. K. Oka and T. Kato, "Spectroscopic polarimetry with a channeled spectrum," Opt. Lett. **24,** 1475–1477 (1999).
28. F. J. Iannarilli, S. H. Jones, H. E. Scott, and P. Kebabian, "Polarimetric-spectral intensity modulation (P-SIM): Enabling simultaneous hyperspectral and polarimetric imaging," Proc. SPIE **3698,** 474–481 (1999).
29. C. J. Bruegge, N. L. Chrien, R. R. Ando, D. J. Diner, W. A. Abdou, M. C. Helmlinger, S. H. Pilorz, and K. J. Thome, "Early validation of the Multi-angle Imaging SpectroRadiometer (MISR) radiometric scale," IEEE Trans. Geosci. Remote Sens. **40,** 1477–1492 (2002).
30. Boulder Nonlinear Systems, "Ferroelectric liquid crystal based polarization filters," http://dev.bouldernonlinear.com/papers/FerroPolarFilters.pdf.
31. C. U. Keller, "Instrumentation for astrophysical spectropolarimetry," in *Astrophysical Spectropolarimetry,* J. Trujillo-Bueno, F. Moreno-Insertis, and F. Sánchez, eds. (Cambridge U. Press, 2002), pp. 303–354.
32. J. O. Stenflo and H. Povel, "Astronomical polarimeter with 2-D detector arrays," Appl. Opt. **24,** 3893–3898 (1985).
33. H. Povel, H. Aebersold, and J. O. Stenflo, "Charge-coupled device image sensor as a demodulator in a 2-D polarimeter with a piezoelastic modulator," Appl. Opt. **29,** 1186–1190 (1990).
34. H. Povel, C. U. Keller, and I.-A. Yadigaroglu, "Two-dimensional polarimeter with a charge-coupled-device image sensor and a piezoelastic modulator," Appl. Opt. **33,** 4254–4260 (1994).
35. A. M. Gandorfer and H. P. Povel, "First observations with a new imaging polarimeter," Astron. Astrophys. **328,** 381–389 (1997).
36. L. D. Landau and E. M. Lifshitz, *Theory of Elasticity,* Vol. 7 of Course of Theoretical Physics, second English ed. (Pergamon, 1970).
37. R. A. Chipman, "Polarimetry," in *Handbook of Optics: Devices, Measurements and Properties,* 2nd ed. M. Bass, ed. (McGraw-Hill, 1994), Vol. II, pp. 1–37.
38. M. Abramowitz and I. A. Stegun, *Handbook of Mathematical Functions* (Dover, 1965).
39. J. O. Stenflo, "Solar magnetic and velocity-field measurements: new instrument concepts," Appl. Opt. **23,** 1267–1278 (1984).
40. J. Bland-Hawthorn and D. H. Jones, "Taurus tunable filter: a flexible approach to narrowband imaging," Publ.-Astron. Soc. Aust. **15,** 44–49 (1998).
41. C. U. Keller, "Charge-caching CMOS detector for polarimetry (C3Po)," Proc. SPIE **5171,** 239–246 (2004).
42. A. M. Gandorfer, "Ferroelectric retarders as an alternative to piezoelastic modulators for use in solar Stokes vector polarimetry," Opt. Eng. **38,** 1402–1408 (1999).